Incorporation of Metal Phosphide Domains into Colloidal Hybrid Nanoparticles

Emil A. Hernández-Pagán,[1,2,*] Robert W. Lord,[1] Joseph M. Veglak,[1] and Raymond E. Schaak[1,3,4,*]

[1] *Department of Chemistry, The Pennsylvania State University, University Park, PA 16802*
[2] *Department of Chemistry and Biochemistry, University of Delaware, Newark, DE 19716*
[3] *Department of Chemical Engineering, The Pennsylvania State University, University Park, PA 16802*
[4] *Materials Research Institute, The Pennsylvania State University, University Park, PA 16802*

Abstract

Colloidal hybrid nanoparticles have generated considerable attention in the inorganic nanomaterials community. The combination of different materials within a single nanoparticle can lead to synergistic properties that can enable new properties, new applications, and the discovery of new phenomena. As such, methodologies for the synthesis of hybrid nanoparticles that integrate metal–metal, metal–chalcogenide, metal–oxide, and oxide–chalcogenide domains have been extensively reported in the literature. However, colloidal hybrid nanoparticles containing metal phosphide domains are rare, despite being attractive systems for their potentially unique catalytic, photocatalytic, and optoelectronic properties. In this Forum article, we report a study of the synthesis of colloidal hybrid nanoparticles that couple the metal phosphides Ni_2P and Co_xP_y with Au, Ag, PbS, and CdS using heterogeneous seeded growth reactions. We also investigate the transformation of Au–Ni heterodimers to Au–Ni_2P, where phosphidation of pre-formed metal–metal hybrid nanoparticles offers an alternative route to metal–phosphide systems. We also study sequential cation exchange reactions to target specific metal–phosphide hybrids, i.e. the transformation of Ni_2P–PbS into Ni_2P–Ag_2S and then Ni_2P–CdS. Throughout all of these pathways, the accompanying discussion emphasizes the synthetic rationale, as well as the challenges in synthesis and characterization that are unique to these systems. In particular, the observation of oxide shells that surround the phosphide domains have implications for the potential photocatalytic applications of these hybrid nanoparticles.

Introduction

It is the year 2021, and inorganic nanoparticles are ubiquitous and mainstream. Gold nanoparticles are used in sensors, semiconductor quantum dots are used in displays, metal oxide nanoparticles are used in sunscreen, magnetic nanoparticles are used in ferrofluids, and the list goes on and on. Each year we learn more and more about the chemistry of how nanoparticles nucleate and grow and how their various property defining features – including size, shape, uniformity, dispersibility, composition, crystal structure, defects, and surface chemistry – can be exquisitely manipulated and tuned. While these features of nanoparticles enable and/or impact their unique size-dependent properties, there are other strategies for modifying their properties as well. One approach is to link them together into larger, yet still discrete, multi-component nanoparticles. Such colloidal hybrid nanoparticles contain two or more material domains, each sharing an interface.[1–3] Integrating nanoparticles into hybrid constructs typically retains the properties of the constituent materials,

but these properties also can be enhanced, modified, or expanded because of their ability to "talk" to each other and interact synergistically.[4]

To date, there are a significant number of colloidal hybrid nanoparticle systems, and many exhibit unique and useful properties.[1–3] One of the most studied systems is CdS–Pt, such as a CdS nanorod with an attached Pt nanoparticle. This hybrid system has been used as a photocatalyst for hydrogen production.[5] The CdS nanorods generate charge carriers from absorption of light. These charge carriers are then transferred to Pt to drive the hydrogen evolution reaction, which is the reduction half reaction of overall water splitting. Replacing the Pt with FePt results in hybrid nanoparticles with magneto-optical properties that can be used for opto-electronic applications such as data storage.[6] Au–Fe_3O_4 has been used as a dual-function magnetic-plasmonic material, with the Fe_3O_4 domain modifying the plasmon resonance of the Au domain,[7] as well as in nanomedicine applications as a theranostic agent for combined MRI contrast (Fe_3O_4) and drug delivery (surface-functionalized Au).[8]

In general, most colloidal hybrid nanoparticles integrate a noble metal or alloy (Au, Ag, Pt, Rh, Pd, Cu, FePt, CoPt) with a metal oxide (Fe_3O_4, ZnO, CoO, In_2O_3, MnO, CeO_{2-x})[9–15] or a metal chalcogenide ($Cu_{2-x}S$, $Cu_{2-x}Se$, PbS, PbSe, CdS, $CuInS_2$, Cu_2ZnSnS_4),[6,7,14–17] although a few other classes exist as well, including metal–metal (Au–Pt, Pt–Ag, Cu–Ag, $CoPt_3$–Au, FePt–Au),[14,18–20] oxide–oxide (TiO_2–Fe_xO_y, TiO_2–VO_2),[21,22] oxide–chalcogenide (Fe_3O_4–CdSe, Fe_2O_3–PbSe),[23,24] and metal–halide (Au–$CsPbBr_3$).[25] Despite this seemingly large number of systems, the functional diversity remains limited. The scope of materials that have been incorporated into colloidal hybrid nanoparticles pales in comparison to the scope of materials for which discrete colloidal nanoparticles can be made, which limits the types of properties that these hybrid constructs can exhibit. One can envision several reasons for this limited scope of colloidal hybrid nanoparticle components. Perhaps it is interest driven, *i.e.,* only those systems which are of interest for their potential multi-functionality or synergistic properties have been targeted, and therefore others just haven't been needed or tried. Perhaps it is synthesis driven, *i.e.,* these are the systems that are easy to make and other systems have bottlenecks that have not yet been overcome. In reality, it is a combination of both of these factors – some systems simply haven't been tried, while others are very challenging (or not yet possible) to make. For example, some of the most valued hybrid nanoparticle targets, such as a Pt–TiO_2–IrO_2 trimer for overall water splitting,[26] remain synthetically elusive because the required materials cannot easily be integrated.

Metal phosphides are a great example of functional materials that remain rare among colloidal hybrid nanoparticles, despite being deposited onto carbon nanomaterials and other high surface area catalytic supports. Metal phosphides, in general, are useful for a wide range of applications, including in energy storage, optoelectronics, catalysis, and biomedicine. As colloidal nanoparticles, metal phosphides have been synthetically accessible for several decades, with several pathways capable of forming them in solution.[27–35] Some of these methods involve arrested precipitation, where metal phosphides precipitate directly from solution. Other methods involve chemical transformation of reactive seed particles, as both our group[31] and the Chiang group[32] described for the synthesis of Ni_2P from the solution-phase reaction of Ni nanoparticles and trioctylphosphine (TOP). Fast forwarding to 2013,[36] we experimentally identified Ni_2P nanoparticles as highly active catalysts for the hydrogen evolution reaction, inspired both by a prior computational prediction[37] and key mechanistic commonalities between hydrogen evolution

and desulfurization, for which Ni_2P was already a well-known catalyst.[38] This discovery positioned Ni_2P (and other related metal phosphides) as inexpensive and Earth-abundant alternatives to Pt for catalyzing hydrogen production in electrolyzers, solar cells, fuel cells, and other clean energy technologies. Overall, a variety of transition metal phosphides have been extensively studied as catalysts for the HER[39–41] and CO_2 reduction,[42] and for decades as hydrogenation[43–45] and hydrodesulfurization[38,46–49] catalysts.

Despite significant advances in the synthesis of metal phosphide nanoparticles, especially in the past few years due to their increasing interest as HER catalysts, they remain rare among colloidal hybrid nanoparticles. Hybrid particles such as Cu–Cu_3P, formed as an intermediate during phosphorization of Cu nanoparticles,[50] have been reported, but seeded growth methods have not generally yielded hybrid phosphide-containing particles. The reason for this is interesting to ponder, because colloidal phosphide nanoparticles are now mainstream, as are colloidal hybrid nanoparticles, and integrating them seems like a logical extension. We have tried in the past to do so, and the successful synthesis of colloidal hybrid nanoparticles containing metal phosphide domains has remained a significant challenge. We postulate several reasons for this. First, the conditions for synthesizing metal phosphide nanoparticles in solution are harsh. Typical phosphorus reagents, including trioctylphosphine (TOP) and tris(trimethylsilyl)phosphine, usually require temperatures in excess of 250 ºC to produce metal phosphide nanoparticle products, although phosphorus, in substoichiometric amounts, can be incorporated at lower temperatures.[51,52] At these high temperatures, the seed particles onto which the phosphides would be grown to produce colloidal hybrid nanoparticles are often unstable. In some cases, the nanoparticle seeds dissolve through leaching and coordination with the phosphine reagent, and in other cases they agglomerate because the integrity of the surface stabilizing ligands becomes compromised or they grow due to Oswald ripening.

As a step toward diversifying and expanding capabilities for the synthesis of colloidal hybrid nanoparticles containing metal phosphide domains, which is a necessary pre-requisite to studying their properties and using them for the aforementioned applications, we considered three pathways. In our first approach, we began by using metal phosphide nanoparticles as seeds to study the growth of other materials. By using the nanoparticle that required the harshest reaction conditions as seeds, *i.e.*, the phosphides, we postulated that the lower reaction temperatures and/or milder conditions required to grow a metal or semiconductor nanoparticle would allow the integrity of the metal phosphide to be maintained. There are challenges to this pathway, though, including the (potentially detrimental) oxide shell that is common and persistent on the metal phosphide nanoparticles, as it significantly modifies the surface chemistry. In our second approach, we began with metal–metal hybrid nanoparticles and studied the use of post-synthetic modification to selectively convert one metal to a metal phosphide through phosphidation with aminophosphine reagents. Here, we leveraged the lower decomposition temperature of aminophosphines for the conversion of Au–Ni hybrids. While this system offers orthogonal reactivity with respect to the hybrid nanoparticle domain that is targeted, the high mobility of Au atoms at elevated temperatures places an upper limit on the reaction temperature, as above 200 ºC Au-containing hybrid nanoparticles can transform to core-shell nanoparticles.[53] In our third approach, we targeted a specific hybrid nanoparticle, Ni_2P–CdS, by first making Ni_2P–PbS, which was accessible using the first approach described above, followed by attempting cation exchange of the PbS domain to post-synthetically transform it to CdS *via* a Ag_2S intermediate. All of the hybrid nanoparticles that

were targeted integrate a HER catalyst (Ni_2P, Co_xP_y) with either a semiconductor (PbS, CdS) or a plasmonic metal (Au, Ag) that can be used in a photocatalytic water splitting system. The three distinct synthetic pathways allowed us to investigate potential routes to colloidal hybrid nanoparticles containing metal phosphide domains, which in the future will likely be important systems for photocatalysis and solar hydrogen generation.

Experimental Section

Chemicals. Dioctyl ether (99%), octadecene (90%), diphenyl ether (99%), oleic acid (90%), oleyalmine (70%), dodecylamine (98%), trioctylamine (98%), trioctylphosphine (TOP, 97%), tributlyphosphine (TBP, 97%), hexaethyltriaminophosphine (HETAP, 97%), cobalt chloride ($CoCl_2$, 97%), trioctylphosphine (99%), gold(III) chloride hydrate ($HAuCl_4 \cdot nH_2O$, 99%), nickel chloride ($NiCl_2$,99.99%), silver triflate (AgOTf, ≥ 99%) cadmium nitrate tetrahydrate [$Cd(NO_3)_2 \cdot 4H_2O$, 98%] were obtained from Sigma-Aldrich. Nickel acetylacetonate [$Ni(acac)_2$, 95%], sulfur powder (325 mesh, 95%), silver nitrate ($AgNO_3$, 99.9%), and lead oxide (PbO, 99.999%) were obtained from Alfa Aesar. Hexanes, ethanol, and isopropanol were obtained from VWR. All materials were used as received without additional purification.

General safety considerations. Air-free Schlenk line (argon) techniques were used throughout the experimental procedure and heating mantles were used to control the temperatures with thermocouples placed inside the flasks. Caution should be exercised as some of the procedures are performed at elevated temperatures under inert atmosphere. Procedures under Ar flow should be monitored carefully as clogging could result in over-pressurizing the Schlenk line. Reactions involving phosphorus reagents have the potential to generate byproducts that are toxic gases, and therefore should be handled entirely in a fume hood.

Synthesis of Ni_2P nanocrystals. Ni_2P nanocrystals were synthesized by modifying previous literature reports,[54,55] as described in the Results and Discussion section. In a typical synthesis, $Ni(acac)_2$ (513.0 mg), dioctyl ether (5.0 mL), and oleylamine (2.0 mL) were combined in a 100 mL 3-neck flask with a stir bar. While stirring, three Ar/vacuum cycles were performed, leaving the flask under Ar. At this point TOP (5.0 mL) was injected, followed by degassing under vacuum at 110 ºC for 30 min. The flask was placed under Ar flow and the temperature was increased to 255 ˚C, where HETAP (1.0 mL) was swiftly injected. After 1 h at 255 ºC, the heating mantle was removed to cool down the flask until reaching room temperature. The particles were purified by three cycles of precipitation with isopropanol:ethanol (7:3) and centrifugation at 13,500 rpm for 3 min, followed by re-suspension in hexanes. The particles were stored in hexanes.

Synthesis of Co_xP_y nanocrystals. The synthesis of Co_xP_y nanocrystals was modified from a previous literature report.[55] In a typical synthesis, $CoCl_2$ (128.8 mg), dodecylamine (10 mL), and oleic acid (1.0 mL) were combined in a 100 mL 3-neck flask and degassed under vacuum at 110 ºC for 30 min with stirring. The flask was placed under Ar flow and the temperature was increased to 255 ºC, at which point HETAP (1.0 mL) was swiftly injected. After 1 h at 255 ºC, the heating mantle was removed to cool down the flask until it reached room temperature. The particles were purified by three cycles of precipitation with warm isopropanol:ethanol (7:3) and centrifugation at 13,500 rpm for 3 min, followed by re-suspension in hexanes. The particles were stored in hexanes.

Synthesis of M_xP_y–PbS hybrid nanocrystals. M_xP_y–PbS heterodimers were synthesized following a reported procedure.[53] PbO (22.3 mg), oleic acid (1.0 mL), and trioctylamine (5.0 mL) were combined in a 50 mL 3-neck flask with a stir bar. The flask was heated to 100 ºC under vacuum with stirring. While the heating was ongoing, the sulfur precursor was prepared by dissolving sulfur powder (12 mg) in oleylamine (0.75 mL) and diphenyl ether (3.0 mL). Once at 100 ºC vacuum was replaced with Ar and the temperature was increased to 120 ºC. At this point, M_xP_y seeds (1.0 mL of a 14-16 mg/mL suspension) were injected. After the temperature recovered to 120 ºC, the sulfur precursor (0.5 mL) was swiftly injected. After 1 h, the heating mantle was removed to cool down the flask until it reached room temperature. The hybrid nanoparticles were purified by two cycles of precipitation with isopropanol and centrifugation at 13,500 rpm for 3 min, followed by re-suspension in hexanes. The particles were stored in hexanes.

Synthesis of M_xP_y–Au hybrid nanocrystals. The synthetic procedure for M_xP_y–Au heterodimers was adapted from previous reports.[53] $HAuCl_4$ (20.0 mg) was transferred to a 50 mL 3-neck flask containing octadecene (5.0 mL), oleylamine (2.0 mL), oleic acid (1.0 mL), and a stir bar. The flask was heated under vacuum to 70 ºC with stirring, then switched to Ar. The M_xP_y nanoparticles (1.0 mL of a 14-16 mg/mL suspension) were injected and the reaction was allowed to proceed for 3 h. The heating mantle was removed to cool down the flask until it reached room temperature. The hybrid nanoparticles were purified by two cycles of precipitation with isopropanol and centrifugation at 13,500 rpm for 3 min, followed by re-suspension in hexanes. The particles were stored in hexanes.

Synthesis of M_xP_y–Ag hybrid nanocrystals. To synthesize M_xP_y–Ag heterodimers, $AgNO_3$ (15.0 mg), oleylamine (2.0 mL), toluene (10.0 mL), and the M_xP_y seeds were combined in a 50 mL 3-neck flask containing a stir bar. The flask was placed under Ar and the temperature was increased to 110 ºC with stirring. After 2 h at this temperature, the flask was cooled down to room temperature by removal of the heating mantle. The hybrid nanoparticles were purified by two cycles of precipitation with isopropanol and centrifugation at 13,500 rpm for 3 min, followed by re-suspension in hexanes. The particles were stored in hexanes.

Synthesis of M_xP_y–CdS hybrid nanocrystals. To synthesize M_xP_y–CdS heterodimers, CdO (12.8 mg), oleic acid (160 µL), and octadecene (5.0 mL), were combined in a 50 mL 3-neck flask containing a stir bar. The flask was placed under Ar and the temperature was increased to 280 ˚C with stirring. At 280 ºC the solution is completely colorless, indicating the formation of $Cd(oleate)_2$. Following the formation of the oleate complex, the temperature is set to 230 ºC. While waiting for the decrease in temperature, the sulfur precursor was prepared by dissolving 16.0 mg of sulfur powder in 10 mL of ODE. Once at 230 ºC, the M_xP_y nanoparticle seeds in octadecene were injected, causing a temperature drop. After the temperature recovered, 1.0 mL of the sulfur precursor was swiftly injected. After 1 h, the heating mantle was removed and the flask was allowed to reach room temperature. The hybrid nanoparticles were purified by two cycles of precipitation with isopropanol and centrifugation at 13,500 rpm for 3 min, followed by re-suspension in hexanes. The particles were stored in hexanes.

Synthesis of Au–Ni hybrid nanocrystals. Au-Ni heterodimers were synthesized by modifying a reported procedure.[56] $HAuCl_4$ (50.0 mg), $NiCl_2$ (111.5 mg), and oleylamine (10.0 mL) were combined in a 50 mL 3-neck flask with a stir bar. While stirring, the temperature was increased to

200 ºC. After 10 min, the heating mantle was removed and the flask was allowed to reach room temperature. The hybrid nanoparticles were purified by two cycles of precipitation with isopropanol and centrifugation at 13,500 rpm for 3 min, followed by re-suspension in hexanes. The particles were stored in hexanes.

Synthesis of Au-Ni_2P via phosphidation. To synthesize Au-Ni_2P via phosphidation, Au-Ni heterodimers (1.0 mL of a 14-16 mg/mL suspension) were transferred to 50 mL 3-neck flask containing oleylamine (6.0 mL) and a stir bar. The flask was heated to 100 ºC under vacuum with stirring. After 30 min, the flask was placed under Ar flow and the temperature was increased to 200 ºC. Once at this temperature, HETAP (500 μL) was swiftly injected and the reaction was allowed to proceed for 1 h. The flask was cooled down to room temperature by removal of the heating mantle. The hybrid nanoparticles were purified by two cycles of precipitation with isopropanol and centrifugation at 13,500 rpm for 3 min, followed by re-suspension in hexanes. The particles were stored in hexanes.

Cation exchange of Ni_2P-PbS. The cation exchange of the heterodimers was adapted and modified from a cation exchange reaction on non-hybrid nanoparticles.[57,58] To access Ni_2P–Ag_2S hybrids, a suspension of Ni_2P–PbS hybrid nanoparticles (12-14 mg) was transferred to a septum capped vial with toluene (5.5 mL) and a stir bar. While stirring, three cycles of Ar/vacuum were performed, after which the vial was left under Ar. The vial was placed in an IPA-dry ice bath (–65 ºC) and after 5 min, 2.5 mL of a 0.05 M AgOTf solution (65mg in 5 mL) in toluene was injected. The vial was removed from the cold bath 5 min after the injection. The exchange reaction was allowed to proceed for another 20 min. The hybrid nanoparticles were purified by two cycles of precipitation with isopropanol and centrifugation at 13,500 rpm for 3 min, followed by re-suspension in toluene. The Ni_2P–Ag_2S particles in toluene were transferred to a septum capped vial with toluene (5 mL) and stir bar. While stirring, 3 cycles of Ar/vacuum were performed, after which the vial was left under Ar. $Cd(NO_3)_2$ (35 mg) dissolved in methanol (1 mL) was injected into the vial followed by tributylphosphine (200 μL). After 1 h at room temperature, the particles were purified by two cycles of precipitation with isopropanol and centrifugation at 13,500 rpm for 3 min, followed by re-suspension in hexanes. The particles were stored in hexanes.

Material Characterization. Transmission electron microscopy (TEM) images, high-resolution transmission electron microscopy (HRTEM) images, high-angle annular dark-field scanning transmission electron microscopy (HAADF-STEM), and STEM energy-dispersive X-ray spectroscopy (STEM-EDS) element maps were collected on an FEI Talos F200X S/TEM at an accelerating voltage of 200 kV. The STEM-EDS element maps for the Co_xP_y-Ag sample were collected on an FEI Titan G2 S/TEM equipped with spherical aberration correctors on the image and probe-forming lenses at an accelerating voltage of 300 kV. The following lines were used to generate the STEM-EDS maps: Ni Kα, Co Kα, Pb Lα, Au Lα, Ag Lα, Cd Lα, P Kα, S Kα, and O Kα. ImageJ software was used for particle size analysis. Bruker ESPIRIT 2 software was used to interpret the STEM-EDS element map data. Powder X-ray diffraction (XRD) data were collected on a Bruker D-8 Advance X-ray diffractometer using Cu Kα radiation. All reference diffraction patterns were simulated based on crystallographic data included in Pearson's Handbook Desk Edition: Crystallographic Data for Intermetallic Phases Vol 1-2.[59,60]

Results and Discussion

Our first approach to synthesize colloidal hybrid nanoparticles containing metal phosphide domains involved heterogeneous nucleation and growth of a semiconductor or metal nanoparticle on the surface of a pre-formed metal phosphide nanocrystal seed. This type of seeded-growth approach is the most common strategy used to synthesize colloidal hybrid nanoparticles, but the incorporation of metal phosphide components has remained challenging. We chose to focus on nickel phosphide (Ni_2P) and cobalt phosphide (Co_xP_y) nanocrystals seeds, since these are two of the most important and widely studied metal phosphide catalysts for the HER,[40] and they have also been investigated for organic transformations.[43,61]

Synthesis of Ni_2P and Co_xP_y nanocrystal seeds

TOP is the most common phosphorus reagent used in the synthesis of colloidal metal phosphide nanocrystals, including through phosphidation of pre-formed metal nanocrystals to transform them to metal phosphides.[30,31] However, aminophosphine reagents are known to produce colloidal metal phosphide nanocrystals at lower reaction temperatures and with shorter reaction times than those required using TOP.[62] We anticipated that both of these characteristics – lower temperatures and shorter reaction times – would be ideal for making metal phosphide nanocrystals for subsequent seeded growth, because they would minimize detrimental surface chemistry modifications, i.e. oxidation or deposition of carbonaceous material.

We were inspired by recent work from Cossairt and co-workers, who used hexaethylaminophosphine (HETAP) as a phosphorus source to produce Ni_2P and Co_xP_y nanocrystals.[55] Their reaction system was simple and elegant – requiring only a metal halide, oleylamine, and an aminophosphine – and this enabled important mechanistic insights. To form Ni_2P nanocrystals using this method, $NiCl_2$ was reduced by oleylamine to form Ni nanocrystals, which were then phosphidized upon injection of HETAP. Brock and co-workers, from whom we also took inspiration, observed an analogous reaction pathway when using $Ni(acac)_2$, oleylamine, dioctyl ether, and TOP.[54] The Ni_2P nanocrystals made using this reaction were uniform in size. We therefore merged these two reactions – HETAP instead of TOP to lower the reaction temperature and time, the bidentate acac ligand instead of chloride for better coordination,[63] and oleylamine and dioctyl ether as complimentary strong and weak coordinating ligands/solvents[63] to help modulate growth and achieve higher morphological uniformity.

XRD and TEM data for the Ni_2P nanocrystal seeds are shown in Figure 1a. The XRD pattern matches well with that expected for Ni_2P nanocrystals, and the TEM images reveal that the particles have a nominally spherical morphology with an average diameter of 7.8 ± 1.0 nm (n = 150). Scherrer analysis of the XRD data yields an average crystalline domain size of 9.5 nm, which is comparable to the TEM data. This procedure was not effective in the synthesis of Co_xP_y, however, because the reaction pathway is different. In the case of cobalt phosphide, $CoCl_2$ (likely complexed with oleylamine) remains in solution until HETAP is injected. At this point the observed color changes from a deep royal blue to black, suggesting the formation of the cobalt phosphide nanocrystal seeds. Addition of oleic acid to the $CoCl_2$–oleylamine reaction mixtures improves the uniformity of the product, yielding cobalt phosphide nanorods with an average length and diameter of 14.9 ± 3.0 nm and 3.8 ± 1.0 nm (n = 150), respectively (Figure 1b). Powder XRD data for the Co_xP_y nanorods (Figure 1b) indicate that they are amorphous, as no peaks

corresponding to a crystalline material are observed. STEM-EDS maps of the hybrid nanoparticles prepared using these Co_xP_y seeds confirm co-localization of Co-P and a slightly cobalt-rich composition. The broad features in the XRD pattern could be attributed to amorphous Co_2P, although an unambiguous determination is not possible.

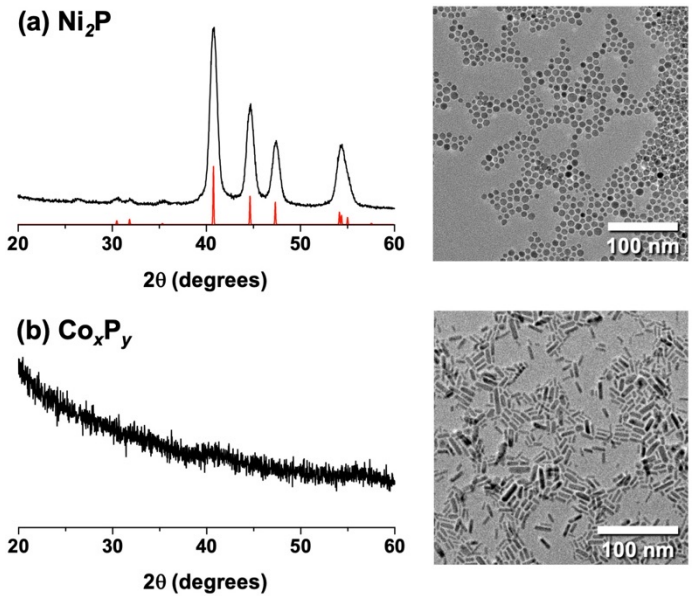

Figure 1. TEM images and XRD patterns for (a) crystalline Ni_2P and (b) amorphous Co_xP_y nanoparticles used for subsequent seeded growth reactions to form hybrid nanoparticles.

Growth of PbS and CdS on Ni_2P and Co_xP_y nanocrystal seeds

Using these Ni_2P and Co_xP_y nanocrystals as seeds, we next targeted the growth of various semiconductors, including PbS and CdS, on their surfaces through heterogeneous seeded growth reactions. These systems were motivated by the desire to understand synthetically how to couple the nickel and cobalt phosphide HER catalysts with light-absorbing semiconductors to produce metal phosphide–semiconductor hybrids, which are of future interest for their potential photocatalytic properties. PbS was chosen because it has a small band gap that allows for absorption of a large portion of the visible spectrum and also because the reaction conditions required to grow it are favorable for accessing hybrid nanoparticles; low growth temperatures decrease the driving force for seed particles to ripen, agglomeration to happen due to ligand instability, and homogeneous nucleation to occur. While PbS can absorb a large portion of the visible spectrum, the position of its conduction band is close to that of the work function of the metal phosphides, which provides limited driving force for electron transfer (Figure S1). For this reason, CdS was also chosen, as it is the prototypical semiconductor used in photocatalytic nanoparticle constructs, *i.e.,* CdS–Pt, and its larger band gap positions the conduction band farther from the work function of the metal phosphides, thereby increasing the driving force for electron transfer.

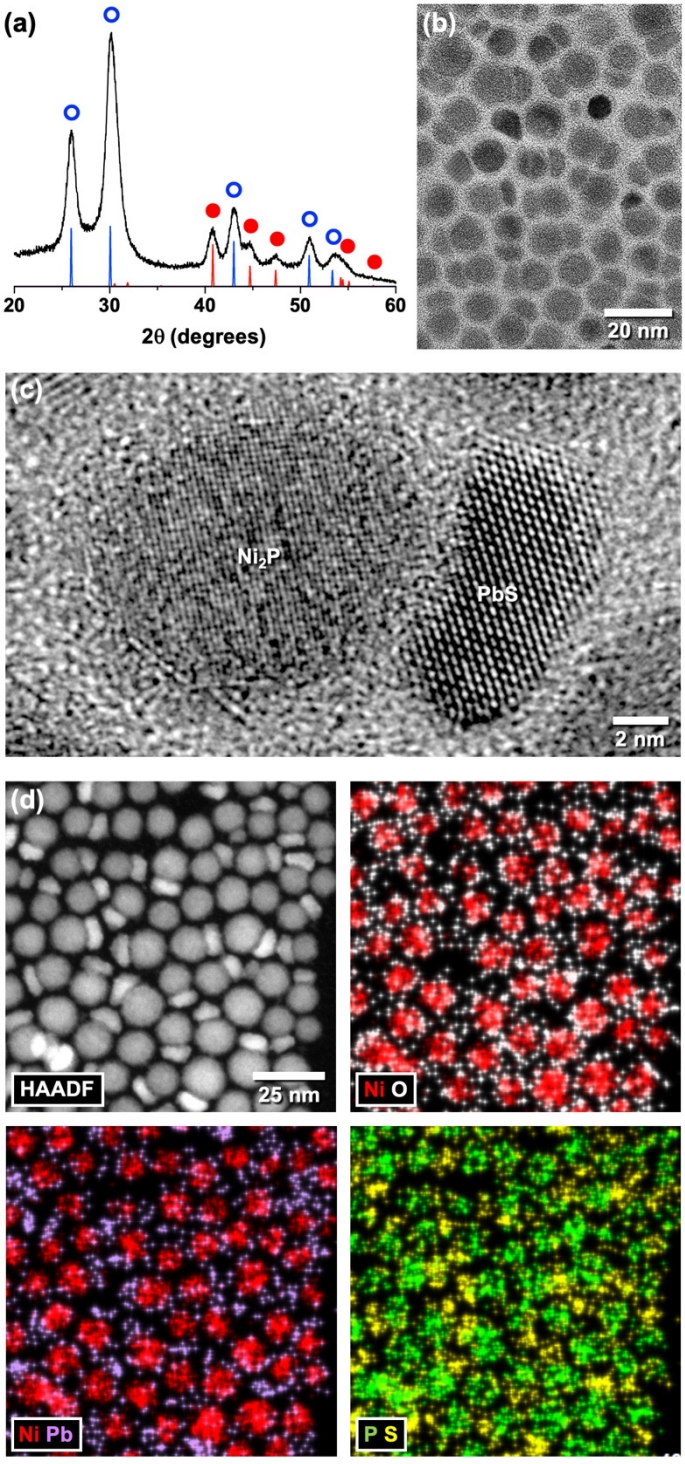

Figure 2. Characterization data for Ni_2P–PbS hybrid nanoparticles. (a) Experimental XRD pattern (black), along with simulated XRD patterns for PbS (blue, open circles) and Ni_2P (red, closed circles) shown for comparison, and (b) TEM image. The HRTEM image in (c) shows the crystallinity of each domain and highlights the amorphous oxide shell surrounding the Ni_2P domain and persisting between the Ni_2P and PbS domains. (d) HAADF-STEM image and

corresponding STEM-EDS element maps showing various combinations of the signals for Ni (red), Pb (purple), P (green), S (yellow), and O (white). Comparison of the maps reveals co-localization of Ni and P, as well as Pb and S. An oxide shell appears to surround the Ni_2P domains.

To synthesize Ni_2P–PbS hybrid nanoparticles, the Ni_2P seeds shown in Figure 1a were injected into a trioctylamine solution of lead oleate at 120 ºC, following by injection of sulfur dissolved in a mixture of oleylamine and diphenyl ether. Powder XRD analysis of the product of this reaction, which produces ~10 mg of isolatable product (as does all of the reactions described herein), showed reflections matching both Ni_2P and PbS (Figure 2a). The TEM images in Figures 2b and S2, along with the HRTEM (Figure 2c) and HAADF-STEM (Figure 2d) images, confirmed that the primary products of this reaction were two-component hybrid nanoparticles, consistent with the targeted Ni_2P–PbS heterodimers. The average Ni_2P and PbS particle sizes by TEM were 10.8 ± 1.6 nm and 9.1 ± 1.8 × 5.7 ± 7 nm, respectively. Scherrer analysis of the XRD data revealed domain sizes of 7.6 nm and 8.1 nm for Ni_2P and PbS, respectively. STEM-EDS element maps (Figure 2d) confirmed the presence of discrete Ni_2P and PbS domains in the hybrid nanoparticles. Closer examination of the TEM and HAADF-STEM images reveals that the Ni_2P and PbS domains are separated by a thin oxide layer that covers the Ni_2P. The presence of the oxide layer is confirmed by the STEM-EDS element map for oxygen, which shows a concentrated oxygen signal surrounding the particles with some co-localization with Ni. This observation is consistent with literature reports describing the surface chemistry of metal phosphides.[39,41,64,65] The HRTEM image shows that both domains are crystalline and that only the Ni_2P domain is surrounded by an amorphous oxide shell. The amorphous oxide layer extends between the Ni_2P and PbS domains, suggesting that it formed *in situ* during synthesis and not during drying. It is therefore possible that PbS could have grown directly on the oxide surface. The presence of an oxide layer suggest a metal-rich surface prone to oxidation. While we will discuss the implications of an oxide layer as it relates to potential photocatalytic applications, this observation highlights several general considerations. First, if a goal is to understand structure-property relationships, then it is important to include in-depth characterization of the surface for catalytic applications where the surface plays a key role. The second consideration involves the handling of the nanoparticles post-synthesis. Most nanoparticle synthesis workup procedures are performed, for convenience, under ambient conditions and the particles are stored on the bench. While this approach works for some applications, we must be mindful that for others, attaining a pristine surface may require use of an air-free workup and storing the particles in the glovebox.

To grow PbS on the Co_xP_y seeds, the procedure was identical to that used to synthesize the Ni_2P–PbS heterodimers, except Co_xP_y seeds were used instead of Ni_2P. Because the Co_xP_y nanocrystal seeds are amorphous, the powder XRD pattern (Figure 3a) for the Co_xP_y–PbS hybrid nanoparticles shows mostly crystalline PbS, although a shoulder near 42º 2θ is consistent with a broad feature noted in the XRD pattern for the Co_xP_y seeds. Figures 3b, 3c, and S3 show HAADF-STEM and HRTEM images for the Co_xP_y–PbS hybrid nanoparticles, along with the corresponding STEM-EDS element maps in Figure 3c. The average PbS particle size by TEM was 7.1 ± 0.9 nm, and Scherrer analysis of the XRD data was 6.3 nm. Seeded growth on nanorods tends to result in the deposition on the new domain at or near the tips of the nanorod, as the tips, which have higher curvature and are more coordinatively unsaturated, have a higher surface energy and a higher reactivity. Consistent with this expectation, the PbS domains tended to grow at or near the tips of

the Co_xP_y nanorods, although some were observed to grow along the sides of the nanorods. As for the Ni_2P–PbS system, an amorphous oxide layer surrounds the Co_xP_y nanorods.

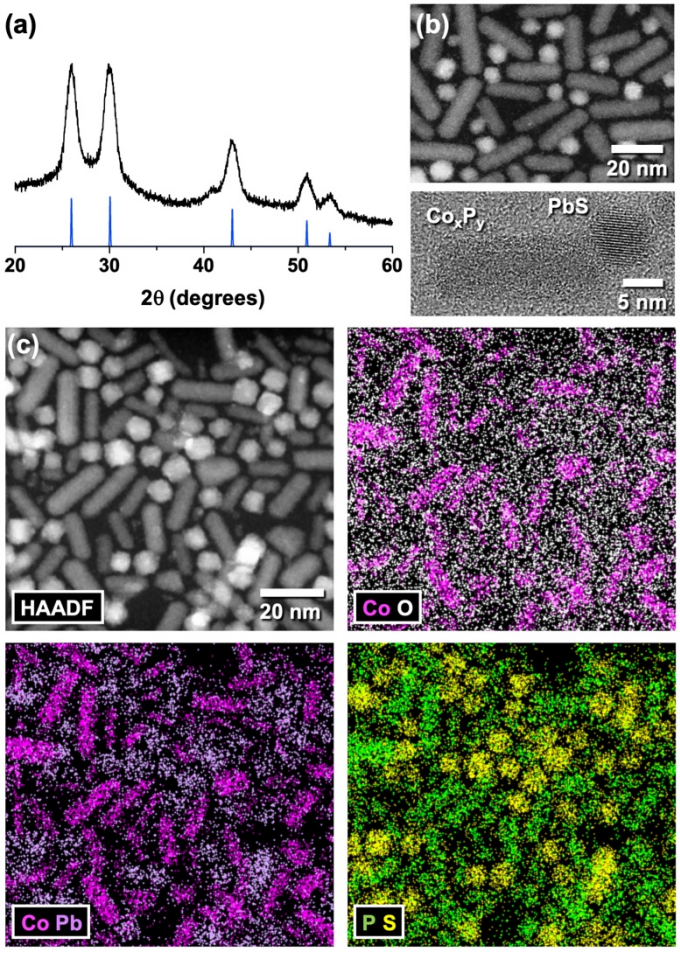

Figure 3. Characterization data for Co_xP_y–PbS hybrid nanoparticles. (a) Experimental XRD pattern (black) with a simulated XRD pattern for PbS shown for comparison. The broad peak near 42º is attributed to the Co_xP_y. (b) HAADF-STEM and HRTEM images of Co_xP_y–PbS hybrid nanoparticles. (c) HAADF-STEM image and corresponding STEM-EDS element maps showing various combinations of the signals for Co (pink), Pb (purple), P (green), S (yellow), and O (white). Comparison of the maps reveals co-localization of Co and P, as well as Pb and S. An oxide shell, which is highlighted in (b), appears to surround the Co_xP_y domains.

To synthesize Ni_2P–CdS hybrid nanoparticles, the Ni_2P seeds shown in Figure 1a were injected into an octadecene solution of cadmium oleate at 250 ºC, followed by injection of sulfur dissolved in octadecene. It should be noted that our target temperature was 235-240 ºC in an effort to avoid homogenous nucleation, as most CdS quantum dot syntheses reported in the literature are carried out above 250 ºC. Therefore, the flask temperature was set to 250 ºC, taking into consideration that the injection of the sulfur reagent would cause a 10-15 ºC drop. Figure 4a shows the powder XRD pattern for the product of this reaction. The observed reflections match well with Ni_2P and

zincblende CdS, which is the polymorph of CdS that is expected to form under these reaction conditions. However, lower-intensity broad reflections near 42º and 50º, as well as shoulders on either side of the most intense peak near 26º, are attributed to a small amount of wurtzite CdS. Figures 4b and S4 show the corresponding TEM images. The HRTEM and HAADF-STEM images in (c) show the amorphous oxide shell that surrounds the Ni_2P domain. The HAADF-STEM image with corresponding STEM-EDS maps in (d) confirm the co-localization of elements that helps lead to the assignment that the two-component heterodimers are Ni_2P–CdS. However, in contrast to Ni_2P–PbS, the CdS domains on Ni_2P–CdS appear as larger, polycrystalline caps. Consistent with this observation, the average dimensions of the CdS domains determined by TEM were 7.7 ± 1.6 nm × 15.5 ± 2.9 nm, while Scherrer analysis of the XRD data indicated an average domain size of 5.0 nm.

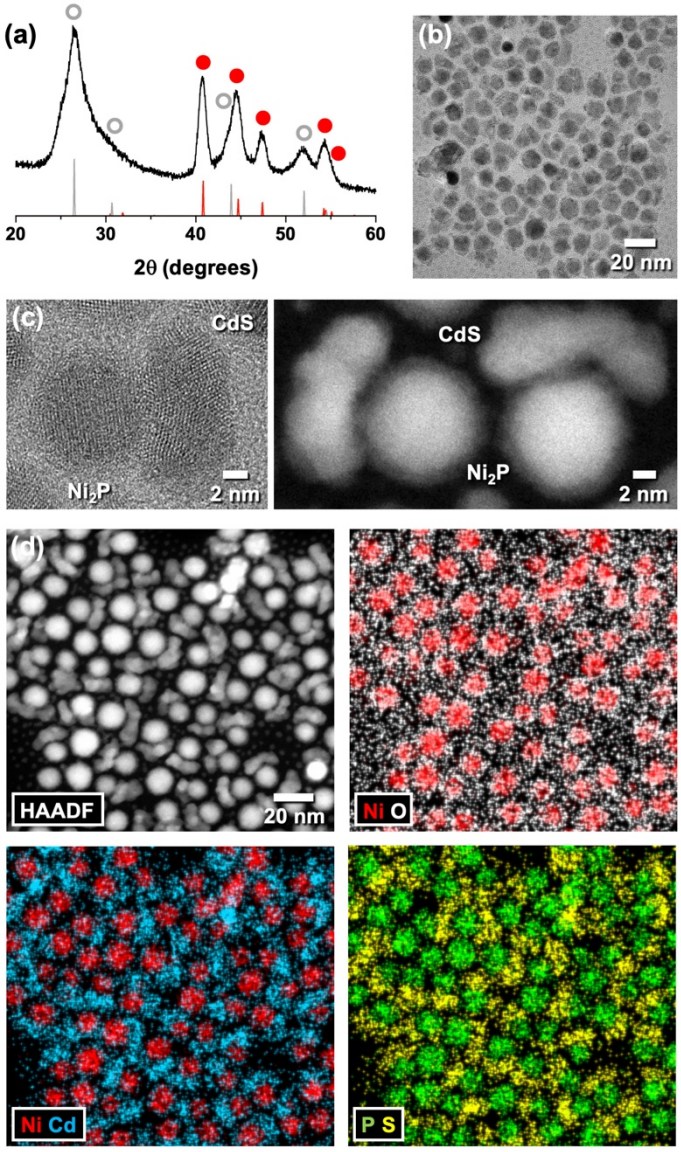

Figure 4. Characterization data for Ni_2P–CdS hybrid nanoparticles. (a) Experimental XRD pattern (black), along with simulated XRD patterns for CdS (gray, open circles) and Ni_2P (red, closed circles) shown for comparison. Broad peaks near 42º and 50º, as well as shoulders on either side

of the most intense peak near 26º, are attributed to a small amount of wurtzite CdS. (b) TEM image of a collection of Ni_2P–CdS hybrid nanoparticles. (c) TEM and HAADF-STEM images of single Ni_2P–CdS hybrid nanoparticles, highlighting the amorphous oxide layer that surrounds the Ni_2P domain. (d) HAADF-STEM image and corresponding STEM-EDS element maps showing various combinations of the signals for Ni (red), Cd (light blue), P (green), S (yellow), and O (white). Comparison of the maps reveals co-localization of Ni and P, as well as Cd and S.

Careful analysis of the TEM images in Figure 4 reveal that, in addition to heterogeneous nucleation and growth of CdS on Ni_2P, homogeneous nucleation and growth of CdS also occurs, as CdS nanoparticles (in the size regime of quantum dots) are present. Attempts to avoid the competing reaction involving homogeneous nucleation and growth of CdS by varying the injection and growth temperatures, the reagent concentrations as well as the sulfur source, were not successful. This is an important point to consider when approaching the synthesis of hybrid nanoparticles having components that undergo competing reactions (i.e. heterogeneous vs homogeneous nucleation and growth) in overlapping temperature regimes. However, given the large size difference between the Ni_2P–CdS hybrid nanoparticles and the CdS quantum dots, size-selective precipitation could be used to separate the two types of particles if desired. Interestingly, no heterogeneous nucleation of CdS was observed when Co_xP_y seeds were used. Instead, only Co_xP_y seeds and free CdS quantum dots were observed (Figure 5). While this result was not what we expected or wanted, and we do not yet understand how the Ni_2P and Co_xP_y surfaces differ, it points to another important issue in heterogeneous seeded growth reactions that are used to synthesize hybrid nanoparticles. The surface chemistry is important for facilitating the nucleation and growth of one particle on another, but details of the nanoparticle surface chemistry are not always known, especially under the reaction conditions where nucleation and growth occur. In general, heterogeneous nucleation will occur at lower temperatures than homogeneous nucleation because there is a lower activation barrier to forming a new surface on an existing surface (i.e. a seed particle) rather than having to first form a new surface (i.e. homogeneous nucleation).[66,67] However, even nuanced and often-unknown details like the level of surface hydration can play a role, as has been reported for Fe_2O_3–PbSe hybrid nanostructures, where heterogeneous nucleation and growth of PbSe was achieved only after surface dehydration of the Fe_2O_3 seeds by heating under vacuum.[24] Systems must be approached on a case-by-case basis, and generalizations are not always possible.

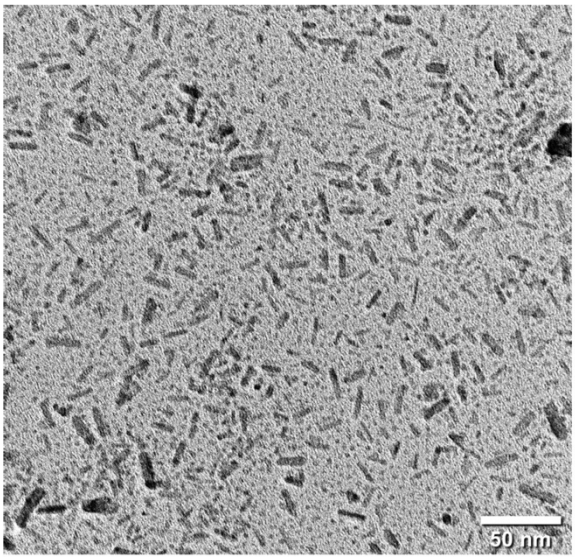

Figure 5. TEM image showing the product obtained after attempting to grow CdS on Co_xP_y. Rod-like Co_xP_y nanoparticles (similar to those in Figure 1b) and CdS quantum dots (small spherical particles) are present, with no evidence of hybrid Co_xP_y–CdS nanoparticles.

The presence of an oxide layer separating the metal phosphide and metal sulfide domains, which was observed in all of the system discussed so far, is interesting and important with respect to the potential photocatalytic applications of these systems. On the one hand, the oxide layer can affect the process of charge transfer from the semiconductor to the catalyst. In dye sensitized solar cells, for example, thin 1-2 nm films of ZrO_2 or Nb_2O_5 films on TiO_2 decreased the rate of back electron transfer between the film and the $[Ru(bpy)_3]^{2+}$ dye.[68] As a result, the efficiency of the solar cell increased. However, thicker oxide layers hindered charge transfer, leading to a decrease in the solar cell efficiency. Ongoing work is focused on studying the charge transfer dynamics in these hybrid systems in order to determine the effects of the oxide layer that separates the two domains. The thickness may be tunable, based on qualitative observations across the different samples made at different temperatures. Conversely, several reports that have used metal phosphides as efficient electrocatalysts for HER and overall water-splitting have observed the presence of a surface oxide on these materials.[39,41,64] This suggest the oxide layer might be beneficial for the catalytic activity and could thus also contribute to the photocatalytic activity of these hybrid systems.

Growth of Au and Ag on Ni_2P and Co_xP_y nanocrystal seeds

In addition to studying the growth of metal sulfide semiconductors on metal phosphide nanocrystal seeds, we also targeted the synthesis of Ni_2P–Au, Co_xP_y–Au, Ni_2P–Ag, and Co_xP_y–Ag. These systems combine the metal phosphide HER catalysts with plasmonic metals, and therefore are useful synthetic targets for plasmon-driven catalysis. We began with the gold systems. In a typical synthesis of Ni_2P–Au or Co_xP_y–Au, the metal phosphide nanocrystal seeds were injected into a flask containing $HAuCl_4$, oleylamine, and oleic acid in octadecene at 70 ºC. Here oleic acid serves as the ligand while oleylamine has the dual role of ligand and reducing agent. The temperature was strategically selected as it is well below that for the homogeneous nucleation and growth of Au nanoparticles. In the absence of seed particles but otherwise identical conditions, Au nanoparticles

start forming at 110 ºC and above. Figure 6 shows XRD, TEM, HAADF-STEM, and STEM-EDS element maps for the resulting Ni_2P–Au and Co_xP_y–Au hybrid nanoparticles; additional TEM data is shown in Figure S5. The domain sizes determined by TEM and Scherrer analysis of the XRD patterns are comparable: 7.5 ± 1.4 for Ni_2P and 6.5 ± 0.7 for Au by TEM and 8.1 nm for Ni_2P and 5.5 nm for Au by XRD. The P signal was omitted from these EDS maps as the Au M X-ray line (2.120 keV) overlaps with the P Kα line (2.013 keV). The Ni_2P–Au hybrids have a heterodimer morphology, while the Co_xP_y–Au hybrids have a matchstick morphology, which is expected due to the nanorod morphology of the Co_xP_y, as discussed above. The Au domains are crystalline in all cases; Ni_2P is also crystalline, while Co_xP_y remains amorphous.

To synthesize the Ag analogues, the appropriate metal phosphide nanocrystal seeds were added to a flask with $AgNO_3$, oleylamine, and toluene, and then the mixture was refluxed for two hours. Ni_2P–Ag and Co_xP_y–Ag exhibit the same morphologies as their Au counterparts, as determined by the TEM image in Figure S6, as well as the HAADF-STEM image and STEM-EDS element maps in Figure 7. The Ag domains are crystalline, based on XRD analysis. The average diameters of the Ni_2P and Ag domains by TEM are 8.1 ± 1.6 nm × 6.8 ± 1.4 nm, respectively, while Scherrer analysis of the XRD data reveals domain sizes of 8.2 and 7.4 nm, respectively. Similar to the metal phosphide–metal sulfide heterodimers, the metal phosphide–noble metal hybrid nanoparticles also contain an oxide shell that surrounds the metal phosphide domains (Figures 6 and 7).

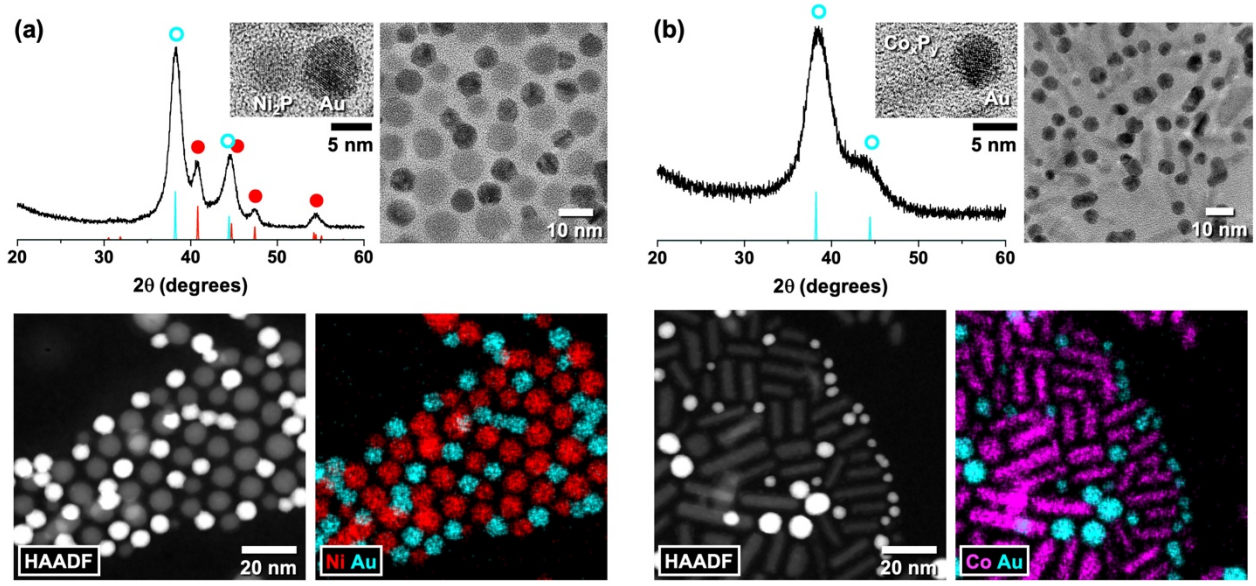

Figure 6. Characterization data for (a) Ni_2P–Au and (b) Co_xP_y–Au hybrid nanoparticles. The top panels for each sample show an experimental XRD pattern (black), along with simulated XRD patterns for Au (cyan, open circles) and Ni_2P (red, closed circles) shown for comparison, as well as TEM images of the hybrid nanoparticles. Co_xP_y is amorphous. The bottom panels show a HAADF-STEM image and a corresponding STEM-EDS element map for each sample. Ni (red) and Au (cyan) are shown for Ni_2P–Au while Co (pink) and Au (cyan) are shown for Co_xP_y–Au. Phosphorus is not shown because the P Kα line overlaps with the Au M line.

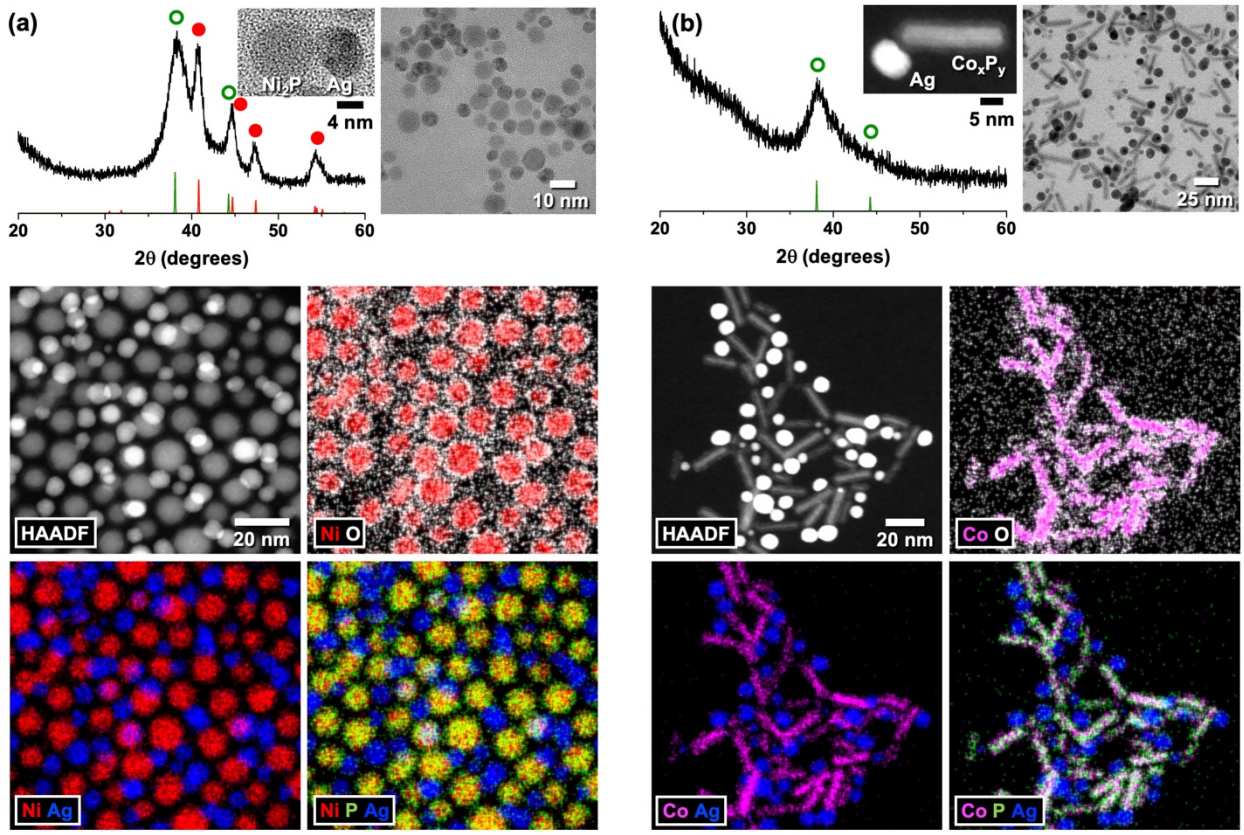

Figure 7. Characterization data for (a) Ni_2P–Ag and (b) Co_xP_y–Ag hybrid nanoparticles. The top panels for each sample show an experimental XRD pattern (black), along with simulated XRD patterns for Ag (green, open circles) and Ni_2P (red, closed circles) shown for comparison, as well as TEM images of the hybrid nanoparticles. Co_xP_y is amorphous. The bottom panels show a HAADF-STEM image and corresponding STEM-EDS element maps for each sample. Ni (red), Ag (blue), P (green), S (yellow), and O (white) are shown for Ni_2P–Ag while Co (pink), Ag (blue), P (green), S (yellow), and O (white) are shown for Co_xP_y–Ag. Comparison of the maps reveals co-localization of Ni and P, Co and P, and Ag and S. An oxide shell appears to surround the phosphide domains.

Post-synthetic modification routes to heterodimers containing metal phosphide domains

While most of our effort in the synthesis of hybrid nanoparticles containing metal phosphide domains focused on heterogeneous nucleation and growth, we also preliminarily explored two alternative post-synthetic modification strategies. These strategies rely on the initial synthesis of template hybrid nanoparticles that pre-define the desired heterodimer morphology, followed by one or more subsequent chemical transformation reactions that selectivity modify one of the hybrid nanoparticle domains to convert it to the desired material. Our first post-synthetic modification pathway focused on a phosphidation reaction. Metal nanoparticles are well known to react at high temperatures in solution with phosphorus reagents, such as TOP and HETAP, to transform them to their corresponding metal phosphides.[69] Such phosphidation reactions have been used previously to transform Ni nanoparticles into Ni_2P.[32,54,69] Accordingly, as a model system, we first synthesized Au–Ni hybrid nanoparticles and studied their transformation to Au–Ni_2P by reacting

them with HETAP at 200 ºC for 1 h. (Gold nanoparticles have also been shown to transform to gold phosphide,[70] but this reaction generally requires higher temperatures than are required for Ni → Ni_2P. The phosphidation reaction, therefore, is effectively selective to the Ni domain, leaving the Au domain unreacted.)

Figure 8 shows XRD, TEM, HAADF-STEM, and STEM-EDS element map data for the Au–Ni nanoparticles, as well as the Au–Ni_2P hybrid nanoparticle products formed through phosphidation. It should be noted that the colocalization of the P and Au signals is a result of the overlap in the X-ray lines, as mentioned previously. While the Au–Ni hybrid nanoparticles did not form in high yield, the XRD data confirms the presence of crystalline Au and Ni, and approximately 50% of the sample consists of Au–Ni heterodimers. Interestingly, the Ni that forms adopts the face centered cubic crystal structure. Ni typically is hexagonally close packed (hcp), so we speculate that the Au nanoparticle seeds, which are fcc, template the growth of the fcc polymorph of Ni. In the phosphidation product, powder XRD data confirms the presence of crystalline Ni_2P, along with Au. Comparison of the HAADF-STEM images and the STEM-EDS element maps before and after the reaction with HETAP indicate that the phosphidation was selective to the Ni domains and that the subpopulation of Au–Ni hybrid nanoparticles transformed to Au–Ni_2P. It is worth noting, however, that the phosphidation reaction did not go to completion across the entire subpopulation of hybrid nanoparticles. Approximately 10% of the Au–Ni heterodimers did not convert to Au–Ni_2P; for these, a Ni_2P shell appears to surround the Ni core, forming a more complex Au–(Ni_2P@Ni) hybrid core-shell particle. The Au–(Ni_2P@Ni) subpopulation included those hybrid nanoparticles having the largest Ni domains, suggesting that higher reaction temperatures may be needed to fully transform them to Ni_2P. We did not optimize, however, as our goal here was to preliminarily evaluate feasibility of the approach as an alternative to heterogeneous seeded growth.

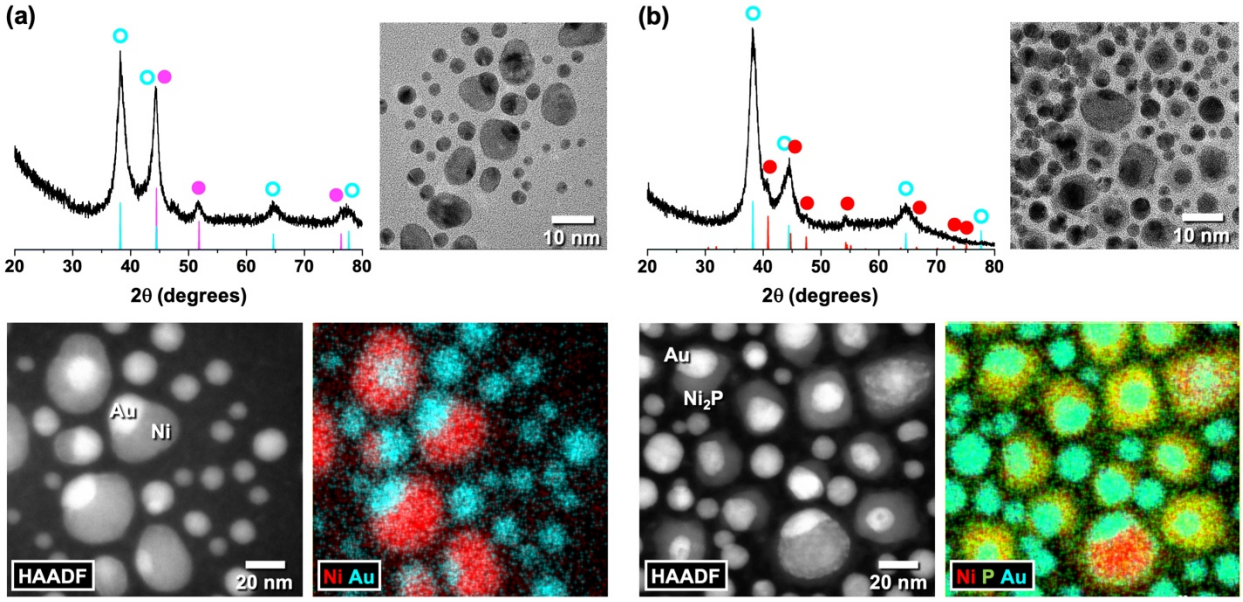

Figure 8. Characterization data for (a) Ni–Au heterodimer seeds and (b) Ni_2P–Au hybrid nanoparticles after phosphidation. The top panels for each sample show a TEM image and an experimental XRD pattern (black), along with simulated XRD patterns for Au (cyan, open circles), fcc Ni (pink closed circles), and Ni_2P (red, closed circles) shown for comparison. The bottom panels show a HAADF-STEM image and a corresponding STEM-EDS element map for each

sample. Ni (red) and Au (cyan) are shown for Ni–Au while Ni (red), Au (cyan), and P (green) are shown for Ni_2P–Au. Note that the P Kα line overlaps with the Au M line, so P and Au appear to be co-localized, although there is no evidence that a gold phosphide phase is present. The largest particle does not fully convert to Ni_2P–Au, but instead forms a Au–(Ni_2P@Ni) hybrid/core-shell particle.

Nanoparticle cation exchange was also studied, preliminarily, as a post-synthetic modification strategy that provides a possible alternative to heterogeneous seeded growth. Here, mobile cations in a nanoparticle (often a metal sulfide) can be replaced by cations in solution to modify composition while maintaining morphology; several review articles describe this chemistry in detail.[71,72] Cation exchange has previously been applied selectively to one domain of a hybrid nanoparticle, i.e. in the transformation of Pt–MnS to Pt–Ag_2S.[11] We used nanoparticle cation exchange to target Ni_2P–CdS, which could not be made through heterogeneous nucleation and growth without also forming a significant amount of CdS quantum dots as an unwanted byproduct, as shown in Figure 4. We therefore approached the formation of Ni_2P–CdS retrosynthetically, using cation exchange pathways. It is known that CdS can be accessed by exchanging the Ag^+ cations of Ag_2S with Cd^{2+}.[73] It is also known that Ag_2S can be accessed by exchanging the Pb^{2+} cations of PbS with Ag^+.[73] Since we already succeeded in making Ni_2P–PbS in high yield through traditional seeded growth methods (see Figure 2), we began with Ni_2P–PbS and carried out sequential, complete cation exchange reactions with Ag^+ and then Cd^{2+}.

Figure 9 shows XRD, TEM, HAADF-STEM, and STEM-EDS element map data for each step of this process, which was approached in a proof-of-concept manner. First, exposure of the Ni_2P–PbS hybrid nanoparticles (shown in Figure 2) to a solution of AgOTf in toluene resulted in a transformation of the rock salt PbS domains into acanthite Ag_2S (Figure 9a). The dimer morphology is retained during the exchange, as is the oxide shell that coats the Ni_2P and persists between the domains of the hybrid nanoparticle. This exchange is extremely favorable energetically and is carried out at –65 ˚C without the addition of any hard base, as is commonly done when exchanging a harder cation with a softer one.[71,72] The Ni_2P–Ag_2S hybrid nanoparticles were then reacted with a methanolic solution of $Cd(NO_3)_2$ in toluene with tributylphosphine (TBP). This exchange is not as energetically favorable and is thus carried out at room temperature with addition of the soft base TBP for solvation of the exiting Ag^+. In contrast to the zincblende CdS domains grown *via* heterogeneous nucleation, the exchange pathway yielded hybrids with wurtzite CdS domains (Figure 9b); an unidentified crystalline impurity was also present in the sample. Crystal structure therefore was not preserved during these cation exchange reactions, as sometimes occurs. However, Pb^{2+} is much larger than the other exchanging cations, and cation exchange reactions involving Pb chalcogenides are not known to retain crystal structure.[74–77] The final exchange, from Ni_2P–Ag_2S to Ni_2P–CdS, appeared to result in some morphological degradation, but the TEM images, particularly near the top of panel b in Figure 9, provide evidence that many heterodimers remained intact.

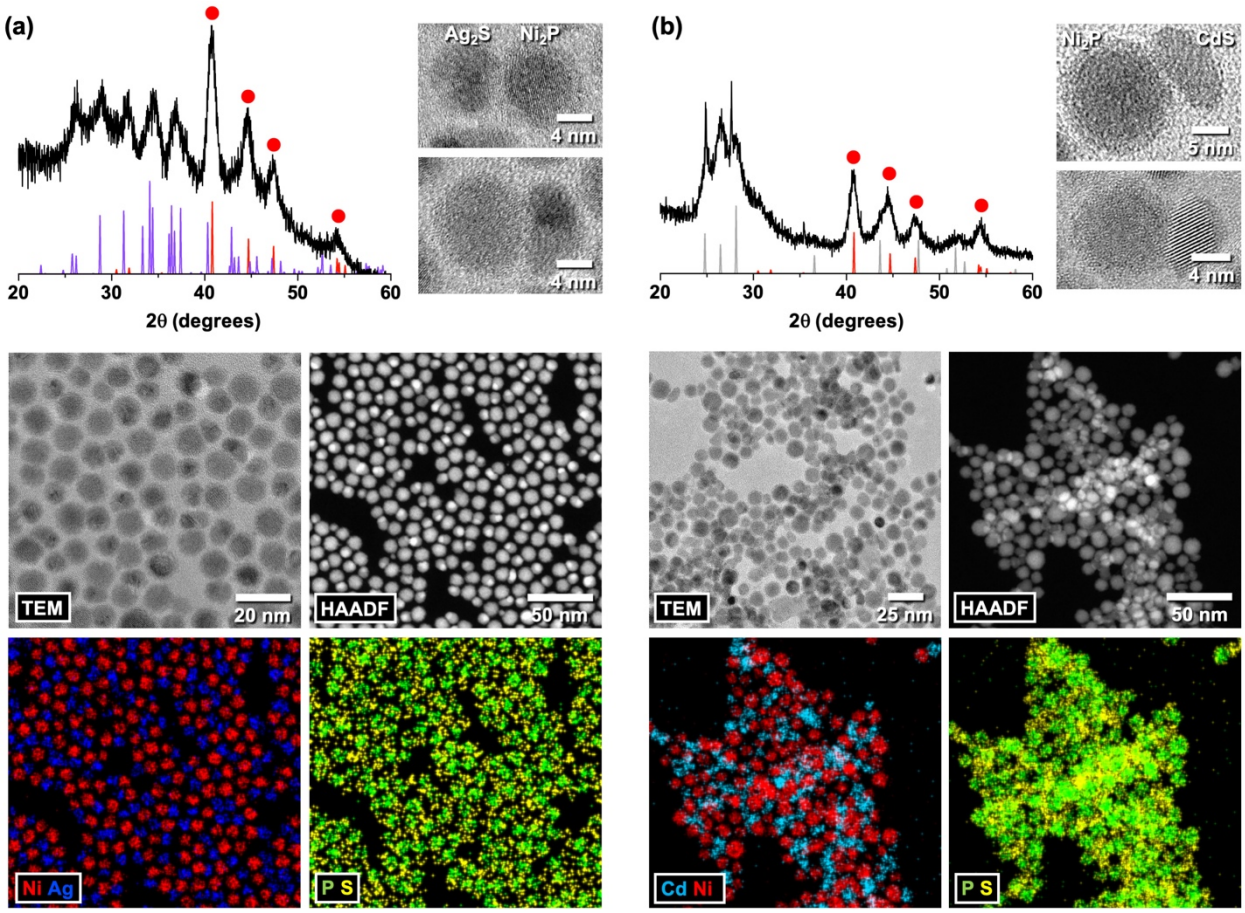

Figure 9. Characterization data for (a) Ni_2P–Ag_2S intermediate formed by cation exchange of the Ni_2P–PbS heterodimers in Figure 2 and (b) the final Ni_2P–CdS hybrid nanoparticles formed after an additional cation exchange reaction. The top panels for each sample show an experimental XRD pattern (black) with simulated XRD patterns for Ag_2S (purple), Ni_2P (red, closed circles), and CdS (gray, open circles) shown for comparison, along with TEM images of the heterodimers, which highlight the persistence of the oxide shell that surrounds the Ni_2P domain. The sharp XRD peaks in (b) come from a small amount of an unidentified crystalline impurity. The bottom panels show a TEM image, HAADF-STEM image, and corresponding STEM-EDS element maps for each sample. Ni (red), Ag (blue), P (green), and S (yellow) are shown for Ni_2P–Ag_2S while Ni (red), Cd (light blue), P (green), and S (yellow) are shown for Ni_2P–CdS. Comparison of the maps reveals co-localization of Ni and P, Ag and S, and Cd and S.

Conclusion

In summary, we studied three synthetic pathways to colloidal hybrid nanoparticles that contain metal phosphide domains. A heterogeneous nucleation approach provided access to Ni_2P–PbS, Ni_2P–CdS, Ni_2P–Au, Ni_2P–Ag, Co_xP_y–PbS, Co_xP_y–Au, and Co_xP_y–Ag. This family of metal phosphide–semiconductor and metal phosphide–plasmonic metal hybrids, which has not previously been synthetically accessible, is of potential interest for photo- and plasmon driven-catalysis. The synthetic insights provided here could therefore be useful for targeting and studying functional hybrid constructs. Phosphidation was also studied for the post-synthetic transformation

of Au–Ni hybrid nanoparticles into Au–Ni_2P by leveraging the lower decomposition temperature of aminophosphines relative to trioctylphosphine. While this particular system displayed orthogonal reactivity, targeting only the Ni domain, further development and extension to other systems could lead to the synthesis of additional asymmetric metal phosphide heterodimers, such as Ni_xP_y–Fe_xP_y. Sequential cation exchange reactions, i.e., the conversion of Ni_2P–PbS to Ni_2P–CdS *via* a Ni_2P–Ag_2S intermediate, was also studied to provide synthetic access to a targeted heterodimer containing a metal phosphide domain. This approach opens up the possibility to access new hybrid constructs with complex heterostructured segments. In depth microscopic analysis of the synthesized systems revealed the presence of an oxide layer on the phosphide domains, which persists across the interface between the metal phosphide and the adjacent domain. This finding highlights the importance of detailed characterization, especially for studies aiming at establishing structure-property relationships.

ASSOCIATED CONTENT

Supporting Information

The Supporting Information is available free of charge on the ACS Publications website.

Additional materials including a band energy level schematic and lower magnification TEM images. Figures S1-S6 (PDF)

Corresponding Authors

Raymond E. Schaak − Department of Chemistry, Department of Chemical Engineering, and Materials Research Institute, The Pennsylvania State University, University Park, Pennsylvania 16802, United States; orcid.org/0000- 0002-7468-8181; E-mail: res20@psu.edu

Emil A. Hernández-Pagán – Department of Chemistry, The Pennsylvania State University, University Park, Pennsylvania 16802, United States. Current address: Department of Chemistry and Biochemistry, University of Delaware, Newark, Delaware 19716, United States; orcid.org/0000-0002-3516-8052; E-mail: emilhp@udel.edu

Author Information

Robert W. Lord − Department of Chemistry, The Pennsylvania State University, University Park, Pennsylvania 16802, United States; orcid.org/0000-0003-1487-1598

Joseph M. Veglak − Department of Chemistry, The Pennsylvania State University, University Park, Pennsylvania 16802, United States

Acknowledgments

This work was supported by the U.S. National Science Foundation under grant CHE-1707830. E.H.P. thanks the Eberly Scholar program at Penn State for support. J.M.V. thanks the Center for

Nanoscale Science (MRSEC) Research Experience for Undergraduates for support. TEM/STEM imaging and EDS mapping were performed at the Materials Characterization Lab of the Penn State Materials Research Institute.

REFERENCES

(1) Banin, U.; Ben-Shahar, Y.; Vinokurov, K. Hybrid Semiconductor-Metal Nanoparticles: From Architecture to Function. *Chem. Mater.* **2014**, *26*, 97–110.
(2) Cortie, M. B.; McDonagh, A. M. Synthesis and Optical Properties of Hybrid and Alloy Plasmonic Nanoparticles. *Chem. Rev.* **2011**, *111*, 3713–3735.
(3) Vaneski, A.; Susha, A. S.; Rodríguez-Fernández, J.; Berr, M.; Jäckel, F.; Feldmann, J.; Rogach, A. L. Hybrid Colloidal Heterostructures of Anisotropic Semiconductor Nanocrystals Decorated with Noble Metals: Synthesis and Function. *Adv. Funct. Mater.* **2011**, *21*, 1547–1556.
(4) Fagan, A. M.; Je, W. R.; Knappenberger, K. L.; Schaak, R. E. Synthetic Control of Hot-Electron Thermalization Efficiency in Size-Tunable Au-Pt Hybrid Nanoparticles. *ACS Nano* **2021**, *15*, 1378-1387.
(5) Amirav, L.; Alivisatos, A. P. Photocatalytic Hydrogen Production with Tunable Nanorod Heterostructures. *J. Phys. Chem. Lett.* **2010**, *1*, 1051–1054.
(6) Shuli, H.; Hongwang, Z.; Savas, D.; Yueling, Q.; Mark, T. S.; Hao, Z. Bifunctional Magneto-Optical FePt-CdS Hybrid Nanoparticles. *J. Phys. Chem. C* **2009**, *113*, 87–90.
(7) Shi, W.; Zeng, H.; Sahoo, Y.; Ohulchanskyy, T. Y.; Ding, Y.; Wang, Z. L.; Swihart, M.; Prasad, P. N. A General Approach to Binary and Ternary Hybrid Nanocrystals. *Nano Lett.* **2006**, *6*, 875–881.
(8) Efremova, M. V.; Naumenko, V. A.; Spasova, M.; Garanina, A. S.; Abakumov, M. A.; Blokhina, A. D.; Melnikov, P. A.; Prelovskaya, A. O.; Heidelmann, M.; Li, Z. A.; Ma, Z.; Shchetinin, I.V.; Golovin, Y.I.; Kireev, I.I.; Savchenko, A.G.; Chekhonin, V.P.; Klyachko, N.L.; Farle, M.; Majouga, A.G.; Wiedwald, U. Magnetite-Gold Nanohybrids as Ideal All-in-One Platforms for Theranostics. *Sci. Rep.* **2018**, *8*, 1–19.
(9) Varandili, S. B.; Huang, J.; Oveisi, E.; De Gregorio, G. L.; Mensi, M.; Strach, M.; Vavra, J.; Gadiyar, C.; Bhowmik, A.; Buonsanti, R. Synthesis of Cu/CeO_{2-x} Nanocrystalline Heterodimers with Interfacial Active Sites to Promote CO_2 Electroreduction. *ACS Catal.* **2019**, *9*, 5035–5046.
(10) Hodges, J. M.; Biacchi, A. J.; Schaak, R. E. Ternary Hybrid Nanoparticle Isomers: Directing the Nucleation of Ag on Pt-Fe_3O_4 Using a Solid-State Protecting Group. *ACS Nano* **2014**, *8*, 1047–1055.
(11) Fenton, J. L.; Hodges, J. M.; Schaak, R. E. Synthetic Deconvolution of Interfaces and Materials Components in Hybrid Nanoparticles. *Chem. Mater.* **2017**, *29*, 6168–6177.
(12) Gordon, T. R.; Schaak, R. E. Synthesis of Hybrid Au-In_2O_3 Nanoparticles Exhibiting Dual Plasmonic Resonance. *Chem. Mater.* **2014**, *26*, 5900–5904.
(13) Wang, C.; Yin, H.; Dai, S.; Sun, S. A General Approach to Noble Metal-Metal Oxide Dumbbell Nanoparticles and Their Catalytic Application for CO Oxidation. *Chem. Mater.* **2010**, *22*, 3277–3282.
(14) Buck, M. R.; Bondi, J. F.; Schaak, R. E. A Total-Synthesis Framework for the Construction of High-Order Colloidal Hybrid Nanoparticles. *Nat. Chem.* **2012**, *4*, 37–44.

(15) Zou, Y.; Sun, C.; Gong, W.; Yang, X.; Huang, X.; Yang, T.; Lu, W.; Jiang, J. Morphology-Controlled Synthesis of Hybrid Nanocrystals via a Selenium-Mediated Strategy with Ligand Shielding Effect: The Case of Dual Plasmonic Au-$Cu_{2-X}Se$. *ACS Nano* **2017**, *11*, 3776–3785.
(16) Hernández-Pagán, E. A.; Leach, A. D. P.; Rhodes, J. M.; Sarkar, S.; Macdonald, J. E. A Synthetic Exploration of Metal-Semiconductor Hybrid Particles of $CuInS_2$. *Chem. Mater.* **2015**, *27*, 7969–7976.
(17) Yu, X.; Shavel, A.; An, X.; Luo, Z.; Ibáñez, M.; Cabot, A. Cu_2ZnSnS_4-Pt and Cu_2ZnSnS_4-Au Heterostructured Nanoparticles for Photocatalytic Water Splitting and Pollutant Degradation. *J. Am. Chem. Soc.* **2014**, *136*, 9236–9239.
(18) Pellegrino, T.; Fiore, A.; Carlino, E.; Giannini, C.; Cozzoli, P. D.; Ciccarella, G.; Respaud, M.; Palmirotta, L.; Cingolani, R.; Manna, L. Heterodimers Based on $CoPt_3$-Au Nanocrystals with Tunable Domain Size. *J. Am. Chem. Soc.* **2006**, *128*, 6690–6698.
(19) Choi, J. S.; Jun, Y. W.; Yeon, S. I.; Kim, H. C.; Shin, J. S.; Cheon, J. Biocompatible Heterostructured Nanoparticles for Multimodal Biological Detection. *J. Am. Chem. Soc.* **2006**, *128*, 15982–15983.
(20) Huang, J.; Mensi, M.; Oveisi, E.; Mantella, V.; Buonsanti, R. Structural Sensitivities in Bimetallic Catalysts for Electrochemical CO_2 Reduction Revealed by Ag-Cu Nanodimers. *J. Am. Chem. Soc.* **2019**, *141*, 2490–2499.
(21) Li, X.; Schaak, R. E. Size- and Interface-Modulated Metal–Insulator Transition in Solution-Synthesized Nanoscale VO_2-TiO_2-VO_2 Heterostructures. *Angew. Chemie - Int. Ed.* **2017**, *56*, 15550–15554.
(22) Buonsanti, R.; Grillo, V.; Carlino, E.; Giannini, C.; Gozzo, F.; Garcia-Hernandez, M.; Garcia, M. A.; Cingolani, R.; Davide Cozzoli, P. Architectural Control of Seeded-Grown Magnetic-Semicondutor Iron Oxide-TiO_2 Nanorod Heterostructures: The Role of Seeds in Topology Selection. *J. Am. Chem. Soc.* **2010**, *132*, 2437–2464.
(23) Tao, K.; Zhou, H.; Dou, H.; Xing, B.; Li, W.; Sun, K. Direct Deposition of Fluorescent Emission-Tunable Cdse on Magnetite Nanocrystals. *J. Phys. Chem. C* **2009**, *113*, 8762–8766.
(24) Selinsky, R. S.; Shin, S.; Lukowski, M. A.; Jin, S. Epitaxial Heterostructures of Lead Selenide Quantum Dots on Hematite Nanowires. *J. Phys. Chem. Lett.* **2012**, *3*, 1649–1656.
(25) Balakrishnan, S. K.; Kamat, P. V. Au-$CsPbBr_3$ Hybrid Architecture: Anchoring Gold Nanoparticles on Cubic Perovskite Nanocrystals. *ACS Energy Lett.* **2017**, *2*, 88–93.
(26) Meekins, B. H.; Kamat, P. V. Role of Water Oxidation Catalyst IrO_2 in Shuttling Photogenerated Holes across TiO_2 Interface. *J. Phys. Chem. Lett.* **2011**, *2*, 2304–2310.
(27) Perera, S. C.; Fodor, P. S.; Tsoi, G. M.; Wenger, L. E.; Brock, S. L. Application of De-Silylation Strategies to the Preparation of Transition Metal Pnictide Nanocrystals: The Case of FeP. *Chem. Mater.* **2003**, *15*, 4034–4038.
(28) Qian, C.; Kim, F.; Ma, L.; Tsui, F.; Yang, P.; Liu, J. Solution-Phase Synthesis of Single-Crystalline Iron Phosphide Nanorods/Nanowires. *J. Am. Chem. Soc.* **2004**, *126*, 1195–1198.
(29) Park, J.; Koo, B.; Yoon, K. Y.; Hwang, Y.; Kang, M.; Park, J. G.; Hyeon, T. Generalized Synthesis of Metal Phosphide Nanorods via Thermal Decomposition of Continuously Delivered Metal-Phosphine Complexes Using a Syringe Pump. *J. Am. Chem. Soc.* **2005**, *127*, 8433–8440.
(30) Henkes, A. E.; Schaak, R. E. Trioctylphosphine: A General Phosphorus Source for the

Low-Temperature Conversion of Metals into Metal Phosphides. *Chem. Mater.* **2007**, *19*, 4234–4242.
(31) Chiang, R. K.; Chiang, R. T. Formation of Hollow Ni_2P Nanoparticles Based on the Nanoscale Kirkendall Effect. *Inorg. Chem.* **2007**, *46*, 369–371.
(32) Wang, J.; Johnston-Peck, A. C.; Tracy, J. B. Nickel Phosphide Nanoparticles with Hollow, Solid, and Amorphous Structures. *Chem. Mater.* **2009**, *21*, 4462–4467.
(33) Trentler, T. J.; Goel, S. C.; Hickman, K. M.; Viano, A. M.; Chiang, M. Y.; Beatty, A. M.; Gibbons, P. C.; Buhro, W. E. Solution-Liquid-Solid Growth of Indium Phosphide Fibers from Organometallic Precursors: Elucidation of Molecular and Nonmolecular Components of the Pathway. *J. Am. Chem. Soc.* **1997**, *119*, 2172–2181.
(34) Buhro, W. E. Metallo-Organic Routes to Phosphide Semiconductors. *Polyhedron* **1994**, *13*, 1131–1148.
(35) Douglas, T.; Theopold, K. H. Molecular Precursors for Indium Phosphide and Synthesis of Small III—V Semiconductor Clusters in Solution. *Inorg. Chem.* **1991**, *30*, 594–596.
(36) Popczun, E. J.; McKone, J. R.; Read, C. G.; Biacchi, A. J.; Wiltrout, A. M.; Lewis, N. S.; Schaak, R. E. Nanostructured Nickel Phosphide as an Electrocatalyst for the Hydrogen Evolution Reaction. *J. Am. Chem. Soc.* **2013**, *135*, 9267–9270.
(37) Liu, P.; Rodriguez, J. A. Catalysts for Hydrogen Evolution from the [NiFe] Hydrogenase to the $Ni_2P(001)$ Surface: The Importance of Ensemble Effect. *J. Am. Chem. Soc.* **2005**, *127*, 14871–14878.
(38) Sawhill, S. J.; Layman, K. A.; Van Wyk, D. R.; Engelhard, M. H.; Wang, C.; Bussell, M. E. Thiophene Hydrodesulfurization over Nickel Phosphide Catalysts: Effect of the Precursor Composition and Support. *J. Catal.* **2005**, *231*, 300–313.
(39) Yan, Y.; Xia, B. Y.; Ge, X.; Liu, Z.; Fisher, A.; Wang, X. A Flexible Electrode Based on Iron Phosphide Nanotubes for Overall Water Splitting. *Chem. - A Eur. J.* **2015**, *21*, 18062–18067.
(40) Callejas, J. F.; Read, C. G.; Roske, C. W.; Lewis, N. S.; Schaak, R. E. Synthesis, Characterization, and Properties of Metal Phosphide Catalysts for the Hydrogen-Evolution Reaction. *Chem. Mater.* **2016**, *28*, 6017–6044.
(41) Xiao, P.; Sk, M. A.; Thia, L.; Ge, X.; Lim, R. J.; Wang, J. Y.; Lim, K. H.; Wang, X. Molybdenum Phosphide as an Efficient Electrocatalyst for the Hydrogen Evolution Reaction. *Energy Environ. Sci.* **2014**, *7*, 2624–2629.
(42) Xu, Y. F.; Duchesne, P. N.; Wang, L.; Tavasoli, A.; Jelle, A. A.; Xia, M.; Liao, J. F.; Kuang, D. Bin; Ozin, G. A. High-Performance Light-Driven Heterogeneous CO_2 Catalysis with near-Unity Selectivity on Metal Phosphides. *Nat. Commun.* **2020**, *11*, 1-8.
(43) Mitsudome, T.; Sheng, M.; Nakata, A.; Yamasaki, J.; Mizugaki, T.; Jitsukawa, K. A Cobalt Phosphide Catalyst for the Hydrogenation of Nitriles. *Chem. Sci.* **2020**, *11*, 6682–6689.
(44) Sweeny, N. P.; Rohrer, C. S.; Brown, O. W. Dinickel Phosphide as a Heterogeneous Catalyst for the Vapor Phase Reduction of Nitrobenzene with Hydrogen to Aniline and Water. *J. Am. Chem. Soc.* **1958**, *80*, 799–800.
(45) Carenco, S.; Leyva-Pérez, A.; Concepción, P.; Boissiere, C.; Mézailles, N.; Sanchez, C.; Corma, A. Nickel Phosphide Nanocatalysts for the Chemoselective Hydrogenation of Alkynes. *Nano Today* **2012**, *7*, 21–28.
(46) Oyama, S. T. Novel Catalysts for Advanced Hydroprocessing: Transition Metal Phosphides. *J. Catal.* **2003**, *216*, 343–352.

(47) Oyama, S. T.; Gott, T.; Zhao, H.; Lee, Y. K. Transition Metal Phosphide Hydroprocessing Catalysts: A Review. *Catal. Today* **2009**, *143*, 94–107.
(48) Oyama, S. T.; Wang, X.; Requejo, F. G.; Sato, T.; Yoshimura, Y. Hydrodesulfurization of Petroleum Feedstocks with a New Type of Nonsulfide Hydrotreating Catalyst. *J. Catal.* **2002**, *209*, 1–5.
(49) Mora-Tamez, L.; Barim, G.; Downes, C.; Williamson, E. M.; Habas, S. E.; Brutchey, R. L. Controlled Design of Phase- and Size-Tunable Monodisperse Ni_2P Nanoparticles in a Phosphonium-Based Ionic Liquid through Response Surface Methodology. *Chem. Mater.* **2019**, *31*, 1552–1560.
(50) Trizio, L. De; Figuerola, A.; Manna, L.; Genovese, A.; George, C.; Brescia, R.; Saghi, Z.; Simonutti, R.; Huis, M. Van; Falqui, A. Size-Tunable, Hexagonal Plate-like Cu_3P and Janus-like Cu-Cu_3P Nanocrystals. *ACS Nano* **2012**, *6*, 32–41.
(51) Moreau, L. M.; Ha, D. H.; Bealing, C. R.; Zhang, H.; Hennig, R. G.; Robinson, R. D. Unintended Phosphorus Doping of Nickel Nanoparticles during Synthesis with TOP: A Discovery through Structural Analysis. *Nano Lett.* **2012**, *12*, 4530–4539.
(52) Carenco, S.; Liu, Z.; Salmeron, M. The Birth of Nickel Phosphide Catalysts: Monitoring Phosphorus Insertion into Nickel. *ChemCatChem* **2017**, *9*, 2318–2323.
(53) Bradley, M. J.; Read, C. G.; Schaak, R. E. Pt-Au Nanoparticle Heterodimers as Seeds for Pt-Au-Metal Sulfide Heterotrimers: Thermal Stability and Chemoselective Growth Characteristics. *J. Phys. Chem. C* **2015**, *119*, 8952–8959.
(54) Muthuswamy, E.; Savithra, G. H. L.; Brock, S. L. Synthetic Levers Enabling Independent Control of Phase, Size, and Morphology in Nickel Phosphide Nanoparticles. *ACS Nano* **2011**, *5*, 2402–2411.
(55) Mundy, M. E.; Ung, D.; Lai, N. L.; Jahrman, E. P.; Seidler, G. T.; Cossairt, B. M. Aminophosphines as Versatile Precursors for the Synthesis of Metal Phosphide Nanocrystals. *Chem. Mater.* **2018**, *30*, 5373–5379.
(56) Wang, D.; Li, Y. One-Pot Protocol for Au-Based Hybrid Magnetic Nanostructures via a Noble-Metal-Induced Reduction Process. *J. Am. Chem. Soc.* **2010**, *132*, 6280–6281.
(57) Son, D. H.; Hughes, S. M.; Yin, Y.; Alivisatos, P. A. Cation Exchange Reactions in Ionic Nanocrystals. *Science* **2004**, *306*, 1009–1012.
(58) Robinson, R. D.; Sadtler, B.; Demchenko, D. O.; Erdonmez, C. K.; Wang, L. W.; Alivisatos, A. P. Spontaneous Superlattice Formation in Nanorods through Partial Cation Exchange. *Science* **2007**, *317*, 355–358.
(59) Villars, P. *Pearson's Hanbook: Desk Edition: Crystallogrpahic Data for Intermetallic Phases, Vol 1*; ASM International: Materials Park, 1997.
(60) Villars, P. *Pearson's Hanbook: Desk Edition: Crystallogrpahic Data for Intermetallic Phases, Vol 2*; ASM International: Materials Park, 1997.
(61) Fujita, S.; Nakajima, K.; Yamasaki, J.; Mizugaki, T.; Jitsukawa, K.; Mitsudome, T. Unique Catalysis of Nickel Phosphide Nanoparticles to Promote the Selective Transformation of Biofuranic Aldehydes into Diketones in Water. *ACS Catal.* **2020**, *10*, 4261–4267.
(62) Tessier, M. D.; De Nolf, K.; Dupont, D.; Sinnaeve, D.; De Roo, J.; Hens, Z. Aminophosphines: A Double Role in the Synthesis of Colloidal Indium Phosphide Quantum Dots. *J. Am. Chem. Soc.* **2016**, *138*, 5923–5929.
(63) Díaz-Torres, R.; Alvarez, S. Coordinating Ability of Anions and Solvents towards Transition Metals and Lanthanides. *Dalt. Trans.* **2011**, *40*, 10742–10750.

(64) Wan, X.; Qian, D.; Ai, L.; Jiang, J. Highly Efficient Peroxymonosulfate Activation by Surface Oxidized Nickel Phosphide with Dual Active Sites. *Ind. Eng. Chem. Res.* **2020**, *59*, 22040-22048.
(65) Zhong, Y.; Yin, L.; He, P.; Liu, W.; Wu, Z.; Wang, H. Surface Chemistry in Cobalt Phosphide-Stabilized Lithium-Sulfur Batteries. *J. Am. Chem. Soc.* **2018**, *140*, 1455–1459.
(66) Thanh, N. T. K.; Maclean, N.; Mahiddine, S. Mechanisms of Nucleation and Growth of Nanoparticles in Solution. *Chem. Rev.* **2014**, *114*, 7610–7630.
(67) Ha, M.; Kim, J. H.; You, M.; Li, Q.; Fan, C.; Nam, J. M. Multicomponent Plasmonic Nanoparticles: From Heterostructured Nanoparticles to Colloidal Composite Nanostructures. *Chem. Rev.* **2019**, *119*, 12208–12278.
(68) Lee, S. H. A.; Zhao, Y.; Hernandez-Pagan, E. A.; Blasdel, L.; Youngblood, W. J.; Mallouk, T. E. Electron Transfer Kinetics in Water Splitting Dye-Sensitized Solar Cells Based on Core-Shell Oxide Electrodes. *Faraday Discuss.* **2012**, *155*, 165–176.
(69) Henkes, A. E.; Vasquez, Y.; Schaak, R. E. Converting Metals into Phosphides: A General Strategy for the Synthesis of Metal Phosphide Nanocrystals. *J. Am. Chem. Soc.* **2007**, *129*, 1896–1897.
(70) Fernando, D.; Nigro, T. A. E.; Dyer, I. D.; Alia, S. M.; Pivovar, B. S.; Vasquez, Y. Synthesis and Catalytic Activity of the Metastable Phase of Gold Phosphide. *J. Solid State Chem.* **2016**, *242*, 182–192.
(71) Beberwyck, B. J.; Surendranath, Y.; Alivisatos, A. P. Cation Exchange: A Versatile Tool for Nanomaterials Synthesis. *J. Phys. Chem. C* **2013**, *117*, 19759–19770.
(72) De Trizio, L.; Manna, L. Forging Colloidal Nanostructures via Cation Exchange Reactions. *Chem. Rev.* **2016**, *116*, 10852–10887.
(73) Morris, A. L.; Lin, C.; Benjamin, S. E.; Devarasetty, V. V. N. M.; Tilluck, W. R.; Lozano, E. I.; Hamo, H.; Aguilar, X. A.; Van Patten, P. G. Toward Improved Scalability of Cation Exchange Reactions of Metal Chalcogenide Nanocrystals. *Chem. Mater.* **2017**, *29*, 6596–6600.
(74) Casavola, M.; Van Huis, M. A.; Bals, S.; Lambert, K.; Hens, Z.; Vanmaekelbergh, D. Anisotropic Cation Exchange in PbSe/CdSe Core/Shell Nanocrystals of Different Geometry. *Chem. Mater.* **2012**, *24*, 294–302.
(75) Lechner, R. T.; Fritz-Popovski, G.; Yarema, M.; Heiss, W.; Hoell, A.; Schülli, T. U.; Primetzhofer, D.; Eibelhuber, M.; Paris, O. Crystal Phase Transitions in the Shell of PbS/CdS Core/Shell Nanocrystals Influences Photoluminescence Intensity. *Chem. Mater.* **2014**, *26*, 5914–5922.
(76) Nelson, A.; Honrao, S.; Hennig, R. G.; Robinson, R. D. Nanocrystal Symmetry Breaking and Accelerated Solid-State Diffusion in the Lead-Cadmium Sulfide Cation Exchange System. *Chem. Mater.* **2019**, *31*, 991–1005.
(77) Gariano, G.; Lesnyak, V.; Brescia, R.; Bertoni, G.; Dang, Z.; Gaspari, R.; De Trizio, L.; Manna, L. Role of the Crystal Structure in Cation Exchange Reactions Involving Colloidal Cu_2Se Nanocrystals. *J. Am. Chem. Soc.* **2017**, *139*, 9583–9590.

For Table of Contents Only

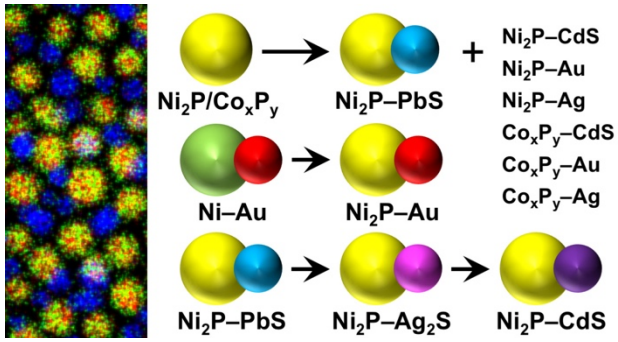

Synposis: Colloidal hybrid nanoparticles that integrate metal phosphides with various metals and semiconductors were synthesized using three complementary strategies. First, Ni_2P and Co_xP_y nanoparticles served as seeds for the growth of PbS, CdS, Au, and Ag. Second, Ni–Au hybrid nanoparticles transformed to Ni_2P–Au through phosphidation. Third, Ni_2P–PbS hybrid nanoparticles transformed to Ni_2P–CdS through sequential cation exchange reactions.